

On the observability of bow shocks of Galactic runaway OB stars

D. M.-A. Meyer,^{1*} A.-J. van Marle,^{2,3} R. Kuiper¹ and W. Kley¹

¹*Institut für Astronomie und Astrophysik, Universität Tübingen, Auf der Morgenstelle 10, 72076 Tübingen, Germany*

²*KU Leuven, Centre for mathematical Plasma Astrophysics, Celestijnenlaan 200B, B-3001 Leuven, Belgium*

³*Laboratoire AstroParticule et Cosmologie - Université Paris 7 Diderot - 10 rue Alice Domon et Léonie Duquet, Paris, 75013, France*

Received January 18 2015; accepted Month day, 2015

ABSTRACT

Massive stars that have been ejected from their parent cluster and supersonically sailing away through the interstellar medium (ISM) are classified as exiled. They generate circumstellar bow shock nebulae that can be observed. We present two-dimensional, axisymmetric hydrodynamical simulations of a representative sample of stellar wind bow shocks from Galactic OB stars in an ambient medium of densities ranging from $n_{\text{ISM}} = 0.01$ up to 10.0 cm^{-3} . Independently of their location in the Galaxy, we confirm that the infrared is the most appropriated waveband to search for bow shocks from massive stars. Their spectral energy distribution is the convenient tool to analyze them since their emission does not depend on the temporary effects which could affect unstable, thin-shelled bow shocks. Our numerical models of Galactic bow shocks generated by high-mass ($\approx 40 M_{\odot}$) runaway stars yield $\text{H}\alpha$ fluxes which could be observed by facilities such as the *SuperCOSMOS H-Alpha Survey*. The brightest bow shock nebulae are produced in the denser regions of the ISM. We predict that bow shocks *in the field* observed at $\text{H}\alpha$ by means of Rayleigh-sensitive facilities are formed around stars of initial mass larger than about $20 M_{\odot}$. Our models of bow shocks from OB stars have the emission maximum in the wavelength range $3 \leq \lambda \leq 50 \mu\text{m}$ which can be up to several orders of magnitude brighter than the runaway stars themselves, particularly for stars of initial mass larger than $20 M_{\odot}$.

Key words: methods: numerical – circumstellar matter – stars: massive.

1 INTRODUCTION

The estimate of massive star feedback is a crucial question in the understanding of the Galaxy’s functioning (Langer 2012). Throughout their short lives, they release strong winds (Holzer & Axford 1970) and ionising radiation (Diaz-Miller et al. 1998) which modify their ambient medium. This results in diaphanous H II regions (Dyson 1975), parsec-scale bubbles of stellar wind (Weaver et al. 1977), inflated (Petrovic et al. 2006) or shed (Woosley et al. 2002; Garcia-Segura et al. 1996) stellar envelopes that impact their close surroundings and which can alter the propagation of their subsequent supernova shock wave (van Veelen 2010; Meyer et al. 2015). Understanding the formation processes of these circumstellar structures allows us to constrain the impact of massive stars, e.g. on the energetics or the chemical evolution of the interstellar medium (ISM). Moreover, it links studies devoted to the dynamical evolution of supernova remnants expanding into the perturbed ISM (Rozyczka et al. 1993) with works focusing on the physics of the star forming ISM (Peters et al. 2010).

While bow-shock-like structures can develop around any as-

trophysical object that moves supersonically with respect to its ambient medium (see e.g. Thun et al. 2016), it particularly affects the surroundings of bright stars running through the ISM (Blaauw 1961). These arc-like structures of swept-up stellar wind material and ISM gas are the result of the distortion of their stellar wind bubble by the bulk motion of their central star (Weaver et al. 1977). Their size and their morphology are governed by their stellar wind mass loss, the wind velocity, the bulk motion of the runaway star and their local ambient medium properties (Comerón & Kaper 1998). These distorted wind bubbles have been first noticed in optical [O III] $\lambda 5007$ spectral emission line around the Earth’s closest runaway star, the OB star ζ Ophiuchi (Gull & Sofia 1979). Other noticeable fast-moving massive stars producing a stellar wind bow shock are, e.g. the blue supergiant Vela-X1 (Kaper et al. 1997), the red supergiant Betelgeuse (Noriga-Crespo et al. 1997) and the very massive star BD+43°365 running away from Cygnus OB2 (Comerón & Pasquali 2007).

Analysis of data from the *Infrared Astronomical Satellite* facility (*IRAS*, Neugebauer et al. 1984) later extended to measures taken with the *Wide-Field Infrared Satellite Explorer* (*WISE*, Wright et al. 2010) led to the compilation of bow shock records, see e.g. (van Buren & McCray 1988). Soon arose the speculation that those isolated nebulae can serve as a tool independent on assump-

* E-mail: dominique.meyer@uni-tuebingen.de

Table 1. Mass M_* (in M_\odot), luminosity L_* (in L_\odot), mass loss \dot{M} (in $M_\odot \text{ yr}^{-1}$) and wind velocity v_w (in km s^{-1}) of our runaway stars at the beginning of the simulations, at a time t_{start} (Myr) after the zero-age main-sequence time. T_{eff} (in K) is the effective temperature of the star at t_{start} . The number of ionizing photons released per unit time S_* (in photon s^{-1}) is taken from Diaz-Miller et al. (1998). Finally, t_{MS} is the main-sequence timescale of the star (in Myr).

M_* (M_\odot)	t_{start} (Myr)	$\log(L_*/L_\odot)$	$\log(\dot{M}/M_\odot \text{ yr}^{-1})$	v_w (km s^{-1})	T_{eff} (K)	S_* (photon s^{-1})	t_{MS} (Myr)
10	5.0	3.80	-9.52	1082	25200	10^{45}	22.5
20	3.0	4.74	-7.38	1167	33900	10^{48}	8.0
40	0.0	5.34	-6.29	1451	42500	10^{49}	4.0

tions regarding the internal physics of these stars, to constrain the still highly debated mass loss of massive stars (Gull & Sofia 1979) and/or their ambient medium density (Huthoff & Kaper 2002). This also raised questions related to the ejection mechanisms of OB stars from young stellar clusters (Hoogerwerf et al. 2001). More recently, multi-wavelengths data led to the publication of the E-BOSS catalog of stellar wind bow shocks (Peri et al. 2012, 2015).

Early simulations discussed the general morphology of the bow shocks around OB stars (Brighenti & D’Ercole 1995, and references therein), their (in)stability (Blondin & Koerwer 1998) and the general incompatibility of the shape of stellar wind bow shocks with analytical approximations such as the one of Wilkin (1996), see in Comerón & Kaper (1998). However, observing massive star bow shocks remains difficult and they are mostly serendipitously noticed in infrared observations of the neighbourhood of stellar clusters (Gvaramadze & Bomans 2008). Moreover, their optical emission may be screened by the H II region which surrounds the driving star and this may affect their H α observations (Brown & Bomans 2005). We are particularly interested in the prediction of the easiest bow shocks to observe, their optical emission properties and their location in the Galaxy.

In the present study, we extend our numerical investigation of the circumstellar medium of runaway massive stars (Meyer et al. 2014, hereafter Paper I). Note that our approach is primarily focussed on exploring the parameter space, rather than a series of simulations tailored to a specific bow shock nebula. Our parameter study explores the effects of the ambient medium density on the emission properties of the bow-like nebulae around the most common runaway stars, in the spirit of works on bow shocks generated by low-mass stars (Villaver et al. 2012, and references therein). The underlying assumptions are the same as in our previous purely hydrodynamical models, i.e. we neglect the magnetisation of the ISM, ignore any intrinsic inhomogeneity in the ISM density field and consider that both the wind and the ISM gas are a perfect gas.

Our paper is organised as follows. In Section 2 we present the numerical methods and the microphysics that is included in our models. The resulting numerical simulations are presented and discussed in Section 3. We then analyze and discuss the emission properties of our bow shock models in Section 4. Finally, we formulate our conclusions in Section 5.

2 METHOD

2.1 Governing equations

The bow shock problem is described in our work by the Euler equations of hydrodynamics. It is a set of equations for mass conservation,

$$\frac{\partial \rho}{\partial t} + \nabla \cdot (\rho \mathbf{v}) = 0, \quad (1)$$

conservation of linear momentum,

$$\frac{\partial \rho \mathbf{v}}{\partial t} + \nabla \cdot (\mathbf{v} \otimes \rho \mathbf{v}) + \nabla p = \mathbf{0}, \quad (2)$$

and conservation of energy,

$$\frac{\partial E}{\partial t} + \nabla \cdot (E \mathbf{v}) + \nabla \cdot (p \mathbf{v}) = \Phi(T, \rho) + \nabla \cdot \mathbf{F}_c, \quad (3)$$

where,

$$E = \frac{p}{(\gamma - 1)} + \frac{\rho v^2}{2}, \quad (4)$$

and where ρ is the mass density of the gas, p its pressure, \mathbf{v} the vector velocity. The temperature of the gas is given by,

$$T = \mu \frac{m_H p}{k_B \rho}, \quad (5)$$

where k_B is the Boltzmann constant and μ is the mean molecular weight, such that $\rho = \mu n m_H$ with n the total number density of the fluid and m_H the mass of a hydrogen atom. The adiabatic index of the gas is $\gamma = 5/3$. The Eq. (3) includes (i) the effects of both the cooling and the heating of the gas by optically-thin radiative processes and (ii) the transport of heat by electronic thermal conduction (see Section 2.3).

2.2 Hydrodynamical simulations

We run two-dimensional, axisymmetric, hydrodynamical numerical simulations using the PLUTO code (Mignone et al. 2007, 2012) in axisymmetric, cylindrical coordinates on a uniform grid $[z_{\text{min}}, z_{\text{max}}] \times [O, R_{\text{max}}]$ of spatial resolution $\Delta = 2.25 \times 10^{-4} \text{ pc cell}^{-1}$ minimum. The stellar wind is injected into the computational domain filling a circle of radius 20 cells centered onto the origin O (see e.g., Comerón & Kaper 1998; Meyer et al. 2014, and references therein). The interaction with the ISM is calculated in the reference frame of the moving star (van Marle et al. 2007, 2011, 2014). Inflowing ISM gas mimicing the stellar motion is set at the $z = z_{\text{max}}$ boundary whereas semi-permeable boundary conditions are set at $z = z_{\text{min}}$ and at $R = R_{\text{max}}$. Wind material is distinguished from the ISM using a passive tracer Q that is advected with the gas and initially set to $Q = 1$ in the stellar wind and to $Q = 0$ in the ISM. The ISM composition is assumed to be solar (Asplund et al. 2009).

The stellar models are calculated using the stellar evolution code of Heger et al. (2005); Yoon & Langer (2005); Petrovic et al. (2005) also described in Brott et al. (2011). It includes the mass loss recipe of Kudritzki et al. (1989) for the main sequence-phase and of de Jager et al. (1988) for the red supergiant phase. The stellar properties are displayed in fig. 3 of Paper I while we summarize the wind properties at the beginning of our simulations in our Table 1.

Table 2. The hydrodynamical models. Parameters M_* (in M_\odot), v_* (in km s^{-1}) and n_{ISM} (in cm^{-3}) are the initial mass of the considered moving star, its space velocity and its local ISM density, respectively.

Model	M_* (M_\odot)	v_* (km s^{-1})	n_{ISM} (cm^{-3})
MS1020n0.01	10	20	0.01
MS1040n0.01	10	40	0.01
MS1070n0.01	10	70	0.01
MS2040n0.01	20	40	0.01
MS2070n0.01	20	70	0.01
MS1020n0.1	10	20	0.10
MS1040n0.1	10	40	0.10
MS1070n0.1	10	70	0.10
MS2020n0.1	20	20	0.10
MS2040n0.1	20	40	0.10
MS2070n0.1	20	70	0.10
MS4070n0.1	40	70	0.10
MS1020n10	10	20	10.0
MS1040n10	10	40	10.0
MS1070n10	10	70	10.0
MS2020n10	20	20	10.0
MS2040n10	20	40	10.0
MS2070n10	20	70	10.0
MS4020n10	40	20	10.0
MS4040n10	40	40	10.0
MS4070n10	40	70	10.0

2.3 Microphysics

In order to proceed on our previous bow shock studies (Paper I, Meyer et al. 2015), we include the same microphysics in our simulations of the circumstellar medium of runaway, massive stars, i.e. we take into account losses and gain of internal energy by optically-thin cooling and heating together with electronic thermal conduction. Optically-thin radiative processes are included into the model using the cooling and heating laws established for a fully ionized medium in Paper I. They are the right-hand term $\Phi(T, \rho)$ of Eq. (3) which is given by,

$$\Phi(T, \rho) = n_{\text{H}}\Gamma(T) - n_{\text{H}}^2\Lambda(T), \quad (6)$$

where $\Gamma(T)$ and $\Lambda(T)$ are the heating and cooling laws, respectively, and n_{H} is the hydrogen number density. It mainly consist of cooling contributions from hydrogen and helium for temperatures $T < 10^6$ K whereas it is principally due to metals for temperatures $T \geq 10^6$ K (Wiersma et al. 2009). A term representing the cooling from collisionally excited forbidden lines (Henney et al. 2009) incorporates the effects of, among other, the [OIII] λ 5007 line emission. The heating contribution includes the reionisation of recombining hydrogen atoms by the starlight (Osterbrock & Bochkarev 1989; Hummer 1994). All our models include electronic thermal conduction (Cowie & McKee 1977). The divergence term in Eq. (3) represents the flux of heat,

$$\mathbf{F}_{\text{c}} = \kappa \nabla T, \quad (7)$$

where κ is the heat conduction coefficient (Spitzer 1962). More details about thermal conduction is also given in Paper I.

2.4 Parameter range

This work consists of a parameter study extending our previous investigation of stellar wind bow shock (Paper I) to regions of the

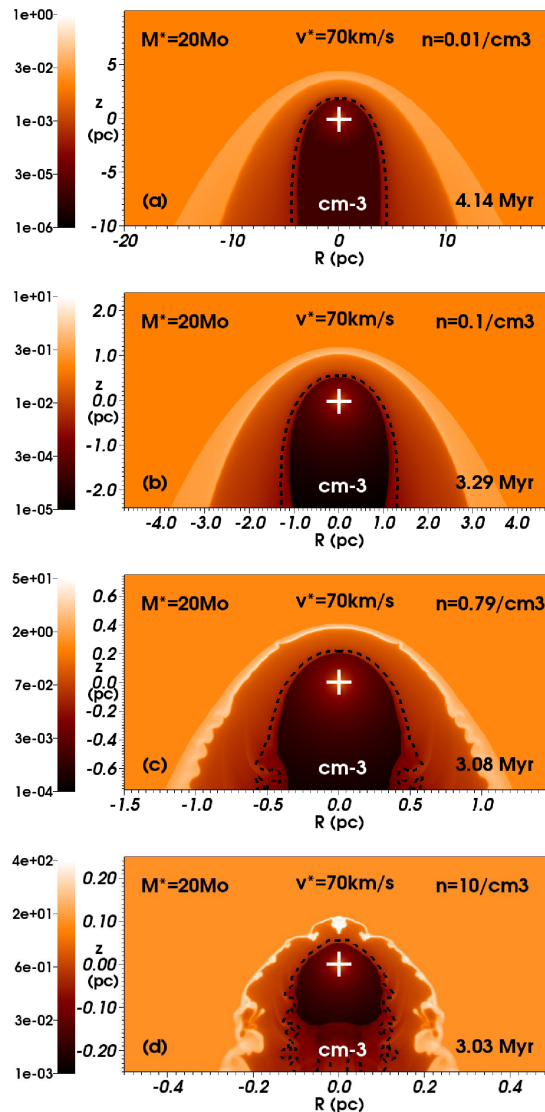


Figure 1. Stellar wind bow shocks from the main sequence phase of the $20 M_\odot$ ZAMS star moving with velocity 70 km s^{-1} as a function of the ISM density, with $n_{\text{ISM}} = 0.01$ (a), 0.1 (b), 0.79 (c) and 10.0 cm^{-3} (d). The gas number density (in cm^{-3}) is shown in the logarithmic scale. The dashed black contour traces the boundary between wind and ISM material. The cross indicates the position of the runaway star. The R -axis represents the radial direction and the z -axis the direction of stellar motion (in pc). Only part of the computational domain is shown.

Galaxy where the ISM has either lower or higher densities. We perform re-runs of the models in Paper I that correspond to the main-sequence phase of our stars, but assume a different ISM background density and only consider the cases where the main-sequence lifetime of the stars is larger than the four crossing times of the gas $|z_{\text{max}} - z_{\text{min}}|/v_*$ through the whole computational domain which are necessary to model steady state bow shocks. The boundary conditions are unchanged, i.e. we consider runaway stars of 10, 20 and $40 M_\odot$ zero-age main-sequence (ZAMS) star moving with velocity $v_* = 20, 40$ and 70 km s^{-1} , respectively. Differences come from the chosen ISM number density that ranges from $n_{\text{ISM}} = 0.01$ to 10.0 cm^{-3} whereas our preceding work exclusively focused on bow shocks models with $n_{\text{ISM}} = 0.79 \text{ cm}^{-3}$. The simulation labels are summarised in Table 2. The analysis of our simulations

include the main-sequence models with $n_{\text{ISM}} = 0.79 \text{ cm}^{-3}$ of Paper I and we refer to them using their original labels.

3 BOW SHOCKS MORPHOLOGY

3.1 Bow shocks structure

In Fig. 1 we show the density fields in our hydrodynamical simulations of our $20 M_{\odot}$ ZAMS star moving with velocity $v_{\star} = 70 \text{ km s}^{-1}$ in a medium of number density $n_{\text{ISM}} = 0.01$ (panel a, model MS2070n0.01), 0.1 (panel b, model MS2070n0.1), 0.79 (panel c, model MS2070) and 10.0 cm^{-3} (panel d, model MS2070n10), respectively. The figures correspond to times about 4.14, 3.29, 3.08 and 3.03 Myr after the beginning of the main-sequence phase. Our bow shocks have the typical structure of a circumstellar nebulae generated by a fast-moving OB star undergoing the conjugated effects of both cooling and heating by optically-thin radiative processes and thermal conduction and the thickness of the shock layer depends on whether the shocks are adiabatic or radiative, which in their turn depends on the shock conditions, see Comerón & Kaper (1998), Paper I and the references therein. All our bow shock simulations have such a structure.

3.2 Bow shocks size

The bow shocks have a stand-off distance $R(0)$, i.e. the distance separating them from the star along the direction of motion predicted by Wilkin (1996). It decreases as a function of (i) v_{\star} , (ii) \dot{M} (c.f. Paper I) and (iii) n_{ISM} since $R(0) \propto n_{\text{ISM}}^{-1/2}$. A dense ambient medium produces a large ISM ram pressure $n_{\text{ISM}} v_{\star}^2$ which results in a compression of the whole bow shock and consequently in a reduction of $R(0)$. As an example, our simulations involving a $20 M_{\odot}$ ZAMS star with $v_{\star} = 70 \text{ km s}^{-1}$ has $R(0) \approx 3.80, 1.14, 0.38$ and 0.07 pc when the driving star moves in $n_{\text{ISM}} = 0.01, 0.1, 0.79$ and 10 cm^{-3} , respectively (Fig. 1a-d), which is reasonably in accordance with Wilkin (1996). All our measures of $R(0)$ are taken at the contact discontinuity, because it is appropriate measure to compare models with Wilkin’s analytical solution (Mohamed et al. 2012).

In Fig. 2 we plot the ratio $R(0)/R(90)$ as a function of the stand-off distance of the bow shocks, where $R(90)$ is the distance between the star and the bow shock measured along the direction perpendicular to the direction of motion. The internal structure of the bow shocks depends on the stellar wind and the bulk motion of the star (Paper I) but are also sensible to the ISM density. Important variations in the stars’ ambient local medium can produce large compression of the region of shocked ISM gas, which in its turn decreases up to form a thin layer of cold shocked ISM gas (see Fig. 1b and fig. 1 of Comerón & Kaper 1998). This phenomenon typically arises in simulations combining moving stars with strong mass loss such as our $40 M_{\odot}$ ZAMS star, together with velocity $v_{\star} \geq 40 \text{ km s}^{-1}$ and/or $n_{\text{ISM}} \geq 1 \text{ cm}^{-3}$ (see large magenta dots in Fig. 2). Those thin-shells are more prone to develop non-linear instabilities (Vishniac 1994; Garcia-Segura et al. 1996).

Interestingly, analytic approximations of the overall shape of a bow shock often assume such an infinitely thin structure (Wilkin 1996) and predict that $R(0)/R(90) = 1/\sqrt{3} \approx 0.58$. Thin shells are very unstable and experience periodical large distortions which can make the shape of the bow shock inconsistent with Wilkin’s prediction of $R(0)/R(90)$ (see black arrows in Fig. 2). Most of

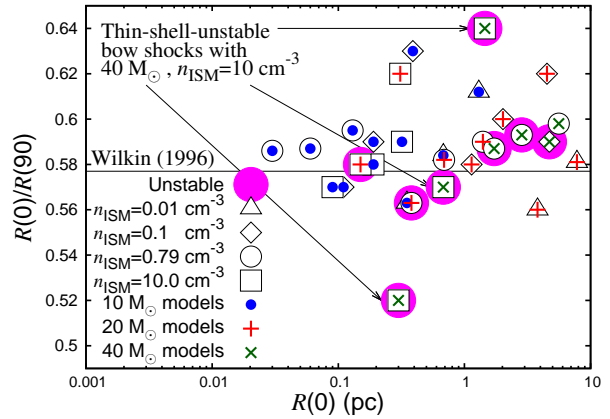


Figure 2. Axis ratio $R(0)/R(90)$ of our bow shock models. The figure shows the ratio $R(0)/R(90)$ measured in the density field of our models measured at their contact discontinuity, as a function of their stand-off distance $R(0)$ (in pc). Symbols distinguish models as a function of (i) the ISM ambient medium with $n_{\text{ISM}} = 0.01$ (triangles), 0.1 (diamonds), 0.79 (circles) and 10.0 cm^{-3} (squares) and (ii) of the initial mass of the star with $10 M_{\odot}$ (blue dots), $20 M_{\odot}$ (blue plus signs) and $40 M_{\odot}$ (dark green crosses), respectively. The thin horizontal black line corresponds to the analytic solution $R(0)/R(90) = 1/\sqrt{3} \approx 0.58$ of Wilkin (1996). The large purple dots highlight the unstable bow shocks.

the models are within 20 per cent of Wilkin’s solution (see horizontal black line at $R(0)/R(90) \approx 1/\sqrt{3}$). Only a few models have $R(0)/R(90) \leq 1/\sqrt{3}$ because their opening is smaller than predicted. However, some simulations with $v_{\star} = 20 \text{ km s}^{-1}$ have large and spread bow shocks in which $R(0)/R(90) \geq 0.62$, see e.g. our simulation MS2020n0.1 with $R(90) \approx 4.51 \text{ pc}$.

3.3 Non-linear instabilities and mixing of material

In Fig. 3 we show a time sequence evolution of the density field in hydrodynamical simulations of $40 M_{\odot}$ zero-age main-sequence star moving with velocity $v_{\star} = 70 \text{ km s}^{-1}$ in a medium of number density $n = 10.0 \text{ cm}^{-3}$ (model MS4070n10). The figures are shown at times 0.02 (a), 0.05 (b), 0.11 (c) and 0.12 Myr (d), respectively. After 0.02 Myr the whole shell is sparsely with small size clumps which are the seeds of non-linear instabilities (Fig. 3b). The fast stellar motion ($v_{\star} = 70 \text{ km s}^{-1}$) provokes a distortion of the bubble into an ovoid shape (see fig. 7 of Weaver et al. 1977) and the high ambient medium density ($n = 10.0 \text{ cm}^{-3}$) induces rapidly a thin shell after only about 0.01 Myr.

The bow shock then experiences a series of cycles in which small scaled eddies grow in the shell (Fig. 3b) and further distort its apex into wing-like structures (Fig. 3c) which are pushed sideways because of the transverse component of the stellar wind acceleration (Fig. 3d). Our model MS4070n10 has both characteristics from the models E ” High ambient density” and G ” Instantaneous cooling” of Comerón & Kaper (1998). Thin-shelled stellar wind bow shocks develop non-linear instabilities, in addition to the Kelvin-Helmholtz instabilities that typically affect interfaces between shearing flows of opposite directions, i.e. the outflowing stellar wind and the ISM gas penetrating the bow shocks (Vishniac 1994; Garcia-Segura et al. 1996; van Marle et al. 2007). A detailed discussion of the development of such non-linearities affecting bow shocks generated by OB runaway stars is in Comerón & Kaper (1998).

In Fig. 4 we plot the evolution of the volume of the bow shock

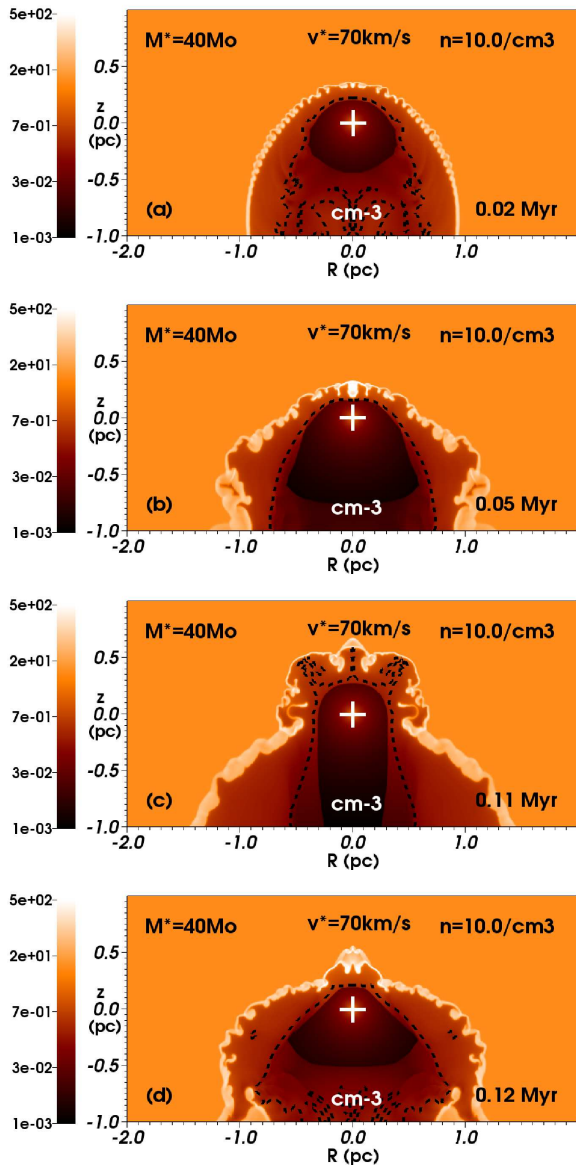


Figure 3. Same as Fig. 1 for our $40 M_{\odot}$ ZAMS star moving through an ISM of density $n_{\text{ISM}} = 10.0 \text{ cm}^{-3}$ with velocity 70 km s^{-1} (model MS4070n10). Figures are shown at times 0.02 (a), 0.05 (b), 0.11 (c) and 0.12 Myr (d) after the beginning of the main sequence phase of the star, respectively. It illustrates the development of the non-linear thin-shell instability in the bow shock.

in our model MS4070n10 (thick solid blue line), separating the volume of shocked ISM gas (thin dotted red line) from the volume of shocked stellar wind (thick dotted orange line) in the apex ($z \geq 0$) of the bow shock. Such a discrimination of the volume of wind and ISM gas is possible because a passive scalar tracer is numerically advected simultaneously with the flow. The figure further illustrates the preponderance of the volume of shocked ISM in the bow shock compared to the stellar wind material, regardless the growth of eddies. Interestingly, the volume of dense shocked ISM gas (large dotted black line) does not have large time variations (see Section 4).

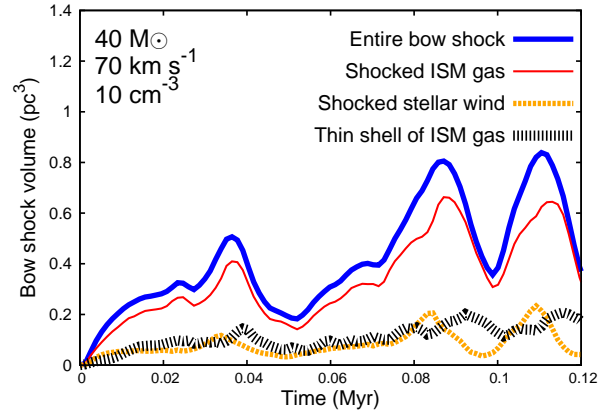


Figure 4. Bow shock volume ($z \geq 0$) in our model MS4070n10 (see Fig. 3a-e). The figure shows the volume of perturbed material (in pc^3) in the computational domain (thick solid blue line), together with the volume of shocked ISM gas (thin solid red line) and shocked stellar wind (thick dotted orange line), respectively, as function of time (in Myr). The large dotted black line represents the volume of the thin shell of shocked ISM.

4 BOW SHOCK ENERGETICS AND EMISSION SIGNATURES

4.1 Methods

In Fig. 5 the total bow shock luminosity L_{total} (pale green diamonds) is calculated integrating the losses by optically-thin radiation in the $z \geq 0$ region of the computational domain (Mohamed et al. 2012, Paper I). Shocked wind emission L_{wind} (orange dots) is discriminated from L_{total} with the help of the passive scalar Q that is advected with the gas, such that,

$$L_{\text{total}} = 2\pi \iint_{z \geq 0} \Lambda(T) n_{\text{H}}^2 R \, dR \, dz, \quad (8)$$

and,

$$L_{\text{wind}} = 2\pi \iint_{z \geq 0} \Lambda(T) n_{\text{H}}^2 Q R \, dR \, dz, \quad (9)$$

respectively. This allows us to isolate the stellar wind material in the bow shock. Additionally, we compute $L_{\text{H}\alpha}$ (blue crosses) and $L_{[\text{OIII}]}$ (dark green triangles) which stand for the bow shock luminosities at $\text{H}\alpha$ and at $[\text{OIII}] \lambda 5007$ spectral line emission using the prescriptions for the emission coefficients in Dopita (1973) and Osterbrock & Bochkarev (1989), respectively. The overall X-ray luminosity L_{X} (black right crosses) is computed with emission coefficients generated with the XSPEC program (Arnaud 1996) with solar metallicity and chemical abundances from Asplund et al. (2009). The total infrared emission L_{IR} (red squares) is estimated as a reemission of a fraction of the starlight bolometric flux on dust grains of gas-to-dust mass ratio 200, which are assumed to be present in the bow shocks. We assume that all dust grains are spherical silicates particles of radius $a = 5.0 \text{ nm}$ only, which are mixed with the gas and continuously penetrate the bow shock as we assume that the star moves with a constant velocity. More details on the dust model and the infrared estimate of the bow shock emission is given in Appendix B of Paper I.

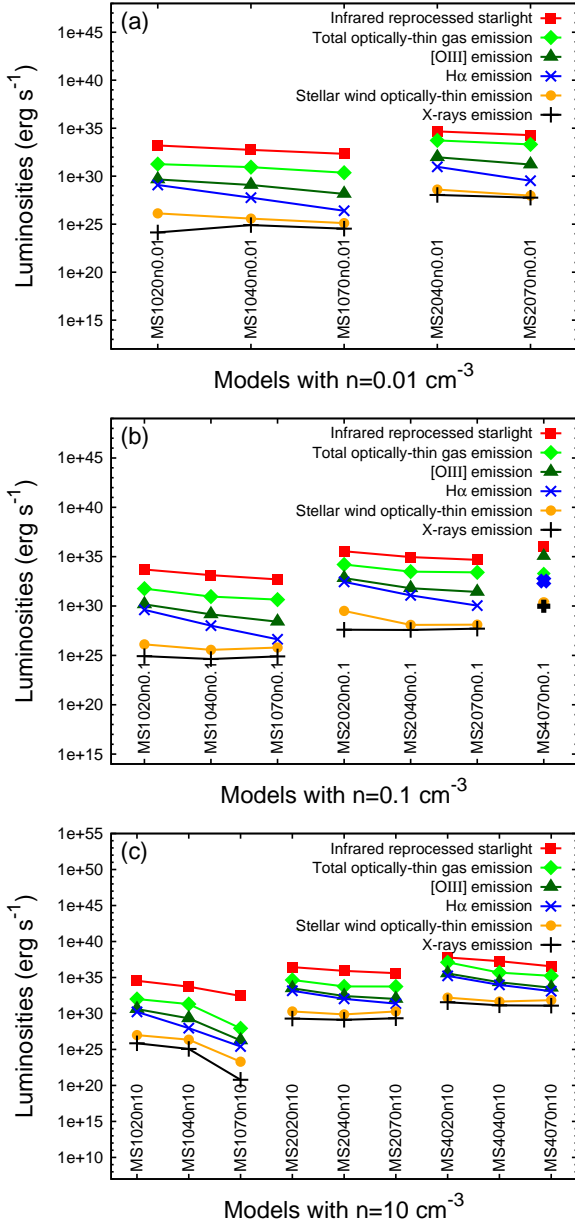


Figure 5. Bow shocks luminosities. The panels correspond to models with an ISM density $n_{\text{ISM}} = 0.01$ (a), 0.1 (b) and 10.0 cm^{-3} (c). The simulations labels are indicated under the corresponding values.

4.2 Results

4.2.1 Optical luminosities

In Fig. 5 we display the bow shocks luminosities as a function of the initial mass of the runaway star, its space velocity v_* and its ambient medium density n_{ISM} . At a given density of the ISM, all of our models have luminosities from optically-thin gas radiation which varies with respect to the stellar mass loss are as described in Paper I for the simulations with $n_{\text{ISM}} \approx 0.79 \text{ cm}^{-3}$. We can identify three major trends for the behaviour of the luminosity:

(i) The total luminosity L_{total} decreases by at least an order of magnitude between the simulations with $v_* = 20$ to 70 km s^{-1} . For example, our $10 M_{\odot}$ ZAMS star, moving with velocity $v_* = 20 \text{ km s}^{-1}$ in an ISM of $n_{\text{ISM}} \approx 0.01 \text{ cm}^{-3}$, has $L_{\text{total}} \approx$

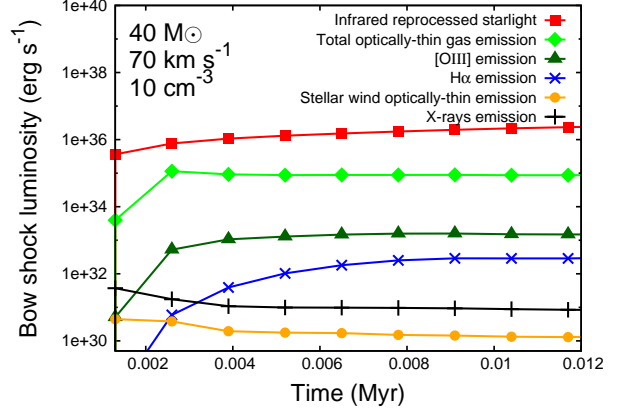


Figure 6. Luminosities of our bow shock simulation of a $40 M_{\odot}$ ZAMS star moving with velocity $v_* = 70 \text{ km s}^{-1}$ through a medium with $n_{\text{ISM}} = 10 \text{ cm}^{-3}$ (see corresponding time-sequence evolution of its density field in Fig. 3a-e). Plotted quantities and color-coding are similar to Fig. 5 and are shown as function of time (in Myr).

$1.82 \times 10^{31} \text{ erg s}^{-1}$ whereas the same star, moving through the same ISM but with velocity $v_* = 70 \text{ km s}^{-1}$, has $L_{\text{total}} \approx 2.29 \times 10^{30} \text{ erg s}^{-1}$ (see models MS1020n0.01 and MS1070n0.01 in Fig 5a). This arises because if the space motion of the star increases the compression factor of the shell of shocked ISM gas in the bow shock, it also reduces its volume which decreases the emission by optical-thin radiative processes (Meyer et al. 2014).

(ii) The total bow shock luminosity by optically-thin processes increases by several orders of magnitude with \dot{M} . For example, the bow shock produced by our $10 M_{\odot}$ ZAMS star moving with velocity $v_* = 40 \text{ km s}^{-1}$ in an ISM of $n_{\text{ISM}} \approx 0.01 \text{ cm}^{-3}$ has $L_{\text{total}} \approx 8.68 \times 10^{30} \text{ erg s}^{-1}$ whereas our $20 M_{\odot}$ ZAMS star moving with the same speed through an identical medium has $L_{\text{total}} \approx 5.38 \times 10^{33} \text{ erg s}^{-1}$ (see models MS1040n0.01 and MS2040n0.01 in Fig 5a). In that sense, our results confirm that the bow shock volume which increases with \dot{M} and decreases with v_* governs their luminosity by optically-thin cooling.

(iii) Finally, the bow shock luminosity decreases if the ambient medium density n_{ISM} increases. This happens because a larger n_{ISM} decreases the volume of the bow shock $\propto R(90)^3$ since $R(90) \propto 1/\sqrt{n_{\text{ISM}}}$, which has a stronger influence over the luminosity than the fact that the density in the post-shock region at the forward shock $\propto n_{\text{ISM}}/4$ increases. For example, the bow shocks generated by our $20 M_{\odot}$ ZAMS star moving with velocity $v_* = 70 \text{ km s}^{-1}$ in an ISM of density $n_{\text{ISM}} = 0.01, 0.1, 0.79$ and 10.0 cm^{-3} have a bow shock luminosity $L_{\text{total}} \approx 2.04 \times 10^{33}, 2.59 \times 10^{33}, 3.72 \times 10^{33}$ and $5.62 \times 10^{33} \text{ erg s}^{-1}$ respectively, see models MS2070n0.01, MS2070n0.1, MS2070 and MS2070n10 (Fig. 1a-d). This further illustrates the dominant role of the bow shock volume on L_{total} , which is governed by the compression of the shell and by the strength of its stellar wind momentum, i.e. \dot{M} and v_w .

The behaviour of the optically-thin emission originating from the shocked stellar wind L_{wind} , the [OIII] $\lambda 5007$ spectral line emission and the $H\alpha$ emission at fixed n_{ISM} are similar as described in Meyer et al. (2014). The contribution of L_{wind} is smaller than L_{total} by several orders of magnitude for all models, e.g. our model MS1020n0.1 has $L_{\text{wind}}/L_{\text{total}} \approx 10^{-5}$. All our models have $L_{H\alpha} < L_{[\text{OIII}]} < L_{\text{total}}$ and the $H\alpha$ emission, the [OIII]

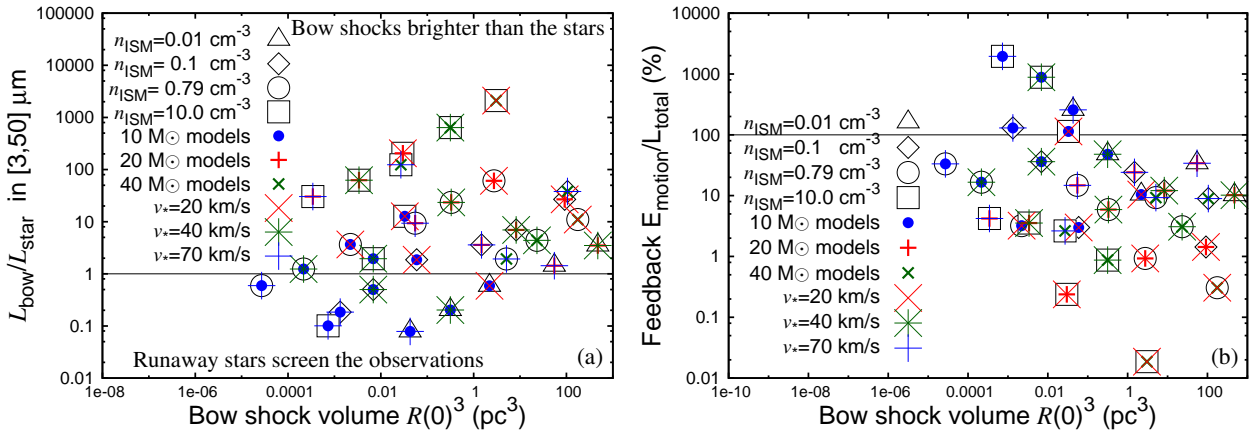


Figure 7. Comparison between the bow shock luminosity of reprocessed starlight $L_{\text{bow}} = L_{\text{IR}}$ and the infrared stellar emission L_* , both in the wavelength range $[3; 50] \mu\text{m}$ (a). Ratio (in %) of the energy deposited per unit time due to the motion of the bow shock with its losses per unit time because of optically-thin cooling (b).

spectral line emission and L_{wind} have variations which are similar to L_{ISM} with respect to M_* , v_* and n_{ISM} .

Fig. 6 shows the lightcurve of our model MS4070n10 computed over the whole simulation and plotted as a function of time with the color coding from Fig. 5. Very little variations of the emission are present at the beginning of the calculation up to a time of about 0.004 Myr and it remains almost constant at larger times. We infer that in the case of a bow shock producing a thin shell of density larger than about 10 cm^{-3} , the distortions of the global structure are largely irrelevant to the luminosity, which is dominated by the dense, shocked, cold ISM gas (see discussion in 4.3). This is in accordance with the volume of the dense ISM gas trapped into the nebula (see large dotted black line in Fig. 4). The independence of L_{IR} with respect to the strong volume fluctuations of thin-shelled nebulae (Fig. 6) indicates that their spectral energy distributions is likely to be the appropriate tool to analyze them since it constitutes an observable which is not reliable to temporary effects.

4.2.2 Infrared and X-rays luminosities

Not surprisingly, the infrared luminosity, which originates from reprocessed starlight on dust grains penetrating the bow shocks, L_{IR} , is larger than L_{total} by about 1 – 2 orders of magnitude. This is possible because the reemission of starlight by dust grains is not taken into account in our simulations. Unlike the optical luminosity, the infrared luminosity increases with n_{ISM} , e.g. our models with $M_* = 10 M_{\odot}$ and $v_* = 20 \text{ km s}^{-1}$ have $L_{\text{IR}} \approx 1.6 \times 10^{33}$, 5.0×10^{33} , 9.92×10^{33} and $3.43 \times 10^{34} \text{ erg s}^{-1}$ if $n_{\text{ISM}} = 0.01$, 0.1 , 0.79 and 10.0 cm^{-3} , respectively. Moreover, the ratio between L_{IR} and L_{total} increases with n_{ISM} , e.g. $L_{\text{IR}}/L_{\text{total}} \approx 8.6$ and 144.1 for the models MS2040n0.01 and MS2040n10, respectively. L_{IR} increases with M_* (Figs. 5a-d). Particularly, we find that $L_{\text{IR}} \gg L_{\text{H}\alpha}$ and $L_{\text{IR}} \gg L_{[\text{OIII}]}$, and therefore we conclude that the infrared waveband is the best way to detect and observe bow shocks from massive main-sequence runaway stars regardless of n_{ISM} (see section 4.3.1).

Note that, according to the prescription for the dust temperature,

$$T_{\text{d}}(r) = T_{\text{eff}} \left(\frac{R_*}{2r} \right)^{\frac{2}{4+s}}, \quad (10)$$

where T_{eff} is the effective temperature of the moving star, R_* its radius and s a parameter giving the slope of the opacity in the infrared regime (Spitzer 1978; Kuiper et al. 2012, and references therein). With $s = 1$ (Decin et al. 2006), it follows that the dust temperature of, e.g. our models with $n_{\text{ISM}} = 0.79 \text{ cm}^{-3}$ is about $T_{\text{d}} \leq 100 \text{ K}$ in the bow shock. The Planck distribution of such temperatures would peak in the mid infrared and therefore one can expect that the dust continuum emission of the bow shocks lies in the wavelength range $3 \leq \lambda \leq 50 \mu\text{m}$. In Fig. 7a we compare the bow shocks and the stellar luminosities in this wavelength range, assuming that the 10 , 20 and $40 M_{\odot}$ ZAMS runaway stars are black bodies. Most of the bow shocks generated by a star of initial mass $\geq 20 M_{\odot}$ are brighter in infrared than their central runaway star. This indicates that bow shocks can dominate the emission up to several orders of magnitude for wavelengths $3 \leq \lambda \leq 50 \mu\text{m}$ and that saturation effects of the observations are improbable for those stars.

Several current and/or planned facilities are designed to observe at these wavelengths and may be able to detect bow shocks from runaway stars:

(i) First, the *James Webb Space Telescope* (JWST) which *Mid-Infrared Instrument* (MIRI, Swinyard et al. 2004) observes in the infrared ($5\text{--}28 \mu\text{m}$) that roughly corresponds to our predicted waveband of dust continuum emission from stellar wind bow shocks of runaway OB stars.

(ii) Secondly, the *Stratospheric Observatory for Infrared Astronomy* (SOFIA) airborne facility which *Faint Object infraRed CAmera for the SOFIA Telescope* (FORCAST, Adams et al. 2008) instrument detects photons in the $5.4\text{--}37 \mu\text{m}$ waveband.

(iii) Then, the proposed *Space Infrared Telescope for Cosmology and Astrophysics* (SPICA, Kaneda et al. 2004) satellite would be the ideal tool to observe stellar wind bow shock, since it is planned to be mounted with (i) a far-infrared imaging spectrometer ($30\text{--}210 \mu\text{m}$), (ii) a mid-infrared coronagraph ($3.5/5\text{--}27 \mu\text{m}$) and (iii) a mid-infrared camera/spectrometer ($5\text{--}38 \mu\text{m}$).

(iv) Finally, we should mention the proposed *The Mid-infrared E-ELT Imager and Spectrograph* (METIS) on the planned *European Extremely Large Telescope* (E-ELT, Brandl et al. 2006), that will be able to scan the sky in the $3\text{--}19 \mu\text{m}$ waveband.

Exploitation of the associated archives of these instruments in re-

gions surroundings young stellar clusters and/or at the locations of previously detected bow-like nebulae (van Buren & McCray 1988; van Buren et al. 1995; Noriega-Crespo et al. 1997; Peri et al. 2012, 2015) are research avenues to be explored.

Finally, we notice that the X-rays emission are much smaller than any other emission lines or bands, e.g. the model MS2070 has $L_X/L_{H\alpha} \approx 10^{-5}$, and it is consequently not a relevant waveband to observe our bow shocks.

4.2.3 Feedback

We compute the energy rate \dot{E}_{motion} deposited to the ISM by the stellar motion. It is estimated by multiplying the rate of volume of ISM swept-up with the bow shock per unit time $\dot{V} \approx \pi R(90)^2 v_*$ by the ISM kinetic energy density defined as $\epsilon_{\text{ISM}} = \rho_{\text{ISM}} \Delta v^2 / 2$, with Δv is the changes in velocity across the shock. In the frame of reference of the moving star $\Delta v = |v_* - v_{\text{gas}}|$, and,

$$\epsilon_{\text{ISM}} = \frac{1}{2} \rho_{\text{ISM}} |v_* - v_{\text{gas}}|^2, \quad (11)$$

where v_{gas} is the gas velocity at the post-shock region at the forward shock. Since the Rankine-Hugoniot relation indicates that $v_{\text{gas}} \approx v_*/4$, then the relation $\dot{E}_{\text{motion}} = \dot{V} \epsilon_{\text{ISM}}$ reduces to,

$$\dot{E}_{\text{motion}} = \frac{9}{32} \rho_{\text{ISM}} v_*^3 \pi R(90)^2, \quad (12)$$

where ρ_{ISM} is the ISM gas mass density.

The ratio $\dot{E}_{\text{motion}}/L_{\text{total}}$ is shown as a function of the bow shock volume in Fig. 7b. The simulations with $M_* \geq 20 M_\odot$ have a bow shock with $\dot{E}_{\text{motion}}/L_{\text{total}} \leq 100\%$ which indicates that their associated nebulae have energy losses by optically-thin radiative processes more important than the energy deposition by the stellar motion itself to the replenishing of the ISM. Our $10 M_\odot$ ZAMS star can produce bow shocks having $\dot{E}_{\text{motion}}/L_{\text{total}} \gg 100\%$. However, since fast-moving $10 M_\odot$ stars are the most common Galactic runaway stars of our sample (Eldridge et al. 2011), it is difficult to estimate which sub-population of runaway massive stars, and by which process, contributes the most to the Galactic feedback. A population synthesis study, beyond the scope of this work, is therefore necessary to assess this question.

4.3 Discussion

4.3.1 The appropriated waveband to observe stellar wind bow shocks in the Galaxy

In Fig. 8 we show the $H\alpha$ surface brightness (in $\text{erg s}^{-1} \text{cm}^{-2} \text{arcsec}^{-2}$, panels a-c) and the infrared luminosity (in erg s^{-1} , panels d-f) for models with $M_* = 10 M_\odot$ (left panels), $20 M_\odot$ (middle panels) and $40 M_\odot$ (right panels). The surface brightness $\Sigma_{H\alpha}^{\text{max}}$ scales with n^2 , see Appendix A of Paper I, therefore the lower the ISM background density of the star, i.e. the higher its Galactic latitude, the fainter the projected emission of the bow shocks and the lower the probability to observe them. The brightest bow shocks are generated both in infrared and $H\alpha$ by our most massive stars running in the denser regions of the ISM ($n_{\text{ISM}} = 10.0 \text{ cm}^{-3}$). The estimate of the infrared luminosity confirms our earlier result relative to bow shock models with $n_{\text{ISM}} = 0.79 \text{ cm}^{-3}$ in the sense that the brightest bow shocks are produced by high-mass, stars (Paper I) moving in a relatively dense ambient medium, i.e. within the Galactic plane (Fig. 8d-f). At $H\alpha$, these bow shocks are associated to fast-moving stars ($v_* = 70 \text{ km s}^{-1}$) producing the strongest

shocks, whereas in infrared they are associated to slowly-moving stars ($v_* = 20 \text{ km s}^{-1}$) generating the largest nebulae.

4.3.2 Synthetic optical emission maps

In Fig. 9 we plot synthetic $H\alpha$ and [OIII] $\lambda 5007$ emission maps of the bow shocks generated by our $20 M_\odot$ ZAMS star moving with velocity 70 km s^{-1} moving through a medium with $n_{\text{ISM}} = 0.1$ (left column of panels), 0.79 (middle column of panels) and 10.0 cm^{-3} (right column of panels). The region of maximum $H\alpha$ emission of the gas is located close to the apex of the bow shock and extended to its trail ($z \leq 0$). This broadening of the emitting region is due to the high space velocity of the star, see Paper I. Neither the shocked stellar wind nor the hot shocked ISM of the bow shock contributes significantly to these emission since the $H\alpha$ emission coefficient $j_{H\alpha} \propto T^{-0.9}$ and the contact discontinuity is the brightest part of the whole structure (Fig. 9a). The [OIII] $\lambda 5007$ emission is maximum at the same location but, however, slightly different dependence on the temperature of the corresponding emission coefficient $j_{[\text{OIII}]} \propto \exp(-1/T)/T^{1/2}$ (Dopita 1973) induces a weaker extension of the emission to the tail of the structure (Fig. 9a). The unstable simulations with $v_* \geq 40 \text{ km s}^{-1}$ and $n_{\text{ISM}} \simeq 10 \text{ cm}^{-3}$ have ring-like artefacts which dominate the emission (see Fig. 9e-h and Fig. 9i-l). They are artificially generated by the over-dense regions of the shell that are rotated and mapped onto the Cartesian grid. A tri-dimensional unstable bow shock would have brighter clumps of matters sparsed around its layer of cold shocked ISM rather than regular rings (Mohamed et al. 2012). Regardless of the properties of their driving star, our bow shocks are brighter in large ambient medium, e.g. the model MS2070n0.1 has $\Sigma_{[H\alpha]}^{\text{max}} \approx 10^{-18} \text{ erg s}^{-1} \text{ cm}^{-2} \text{ arcsec}^{-2}$ whereas the model MS2070n10 has $\Sigma_{[H\alpha]}^{\text{max}} \approx 3 \times 10^{-15} \text{ erg s}^{-1} \text{ cm}^{-2} \text{ arcsec}^{-2}$. The projected [OIII] $\lambda 5007$ emission behaves similarly.

In Fig. 10 we show cross-sections of the $H\alpha$ surface brightness of the model MS2070n0.1. The cuts are taken along the symmetry axis of the figures and plotted as a function of the inclination angle ϕ with respect to the plane of the sky. The emission rises slightly as ϕ increases from for $\phi = 30^\circ$ (thin red solid line) to $\phi = 60^\circ$ (thick solid orange line) since $\Sigma_{[H\alpha]}^{\text{max}}$ peaks at about 6×10^{-19} and about $10^{-18} \text{ erg s}^{-1} \text{ cm}^{-2} \text{ arcsec}^{-2}$, respectively. The case with $\phi = 90^\circ$ is different since the emission decreases to about $\approx 2 \times 10^{-19} \text{ erg s}^{-1} \text{ cm}^{-2} \text{ arcsec}^{-2}$ (see thick dotted green line in Fig. 10). The same is true for the [OIII] emission since its dependence on the post-shock density is similar. These differences arise because a line-of-sight corresponding to $\phi = 60^\circ$ intercepts a larger amount of dense, emitting material in the layer of shocked ISM than a line-of-sight corresponding to $\phi \leq 30^\circ$ or $\phi = 90^\circ$. Large angles of inclination make the opening of the bow shocks larger (Fig. 10a-c, e-g, i-k) and the stand-off distance appears smaller (Fig. 10a-c). Note that bow shocks observed with a viewing angle of $\phi = 90^\circ$ do not resemble an arc-like shape but rather an overlapping of iso-emitting concentric circles (Fig. 10d,h,l).

4.3.3 Bow shocks observability at $H\alpha$ and comparison with observations

In Fig. 11 we show our bow shocks' $H\alpha$ surface brightness (a) and their $\Sigma_{[\text{OIII}]}^{\text{max}}/\Sigma_{[H\alpha]}^{\text{max}}$ ratio (b), both as a function of the volume of emitting gas ($z \geq 0$). The color coding of both panels takes over the definitions adopted in Fig. 2. The models with a $10 M_\odot$ ZAMS

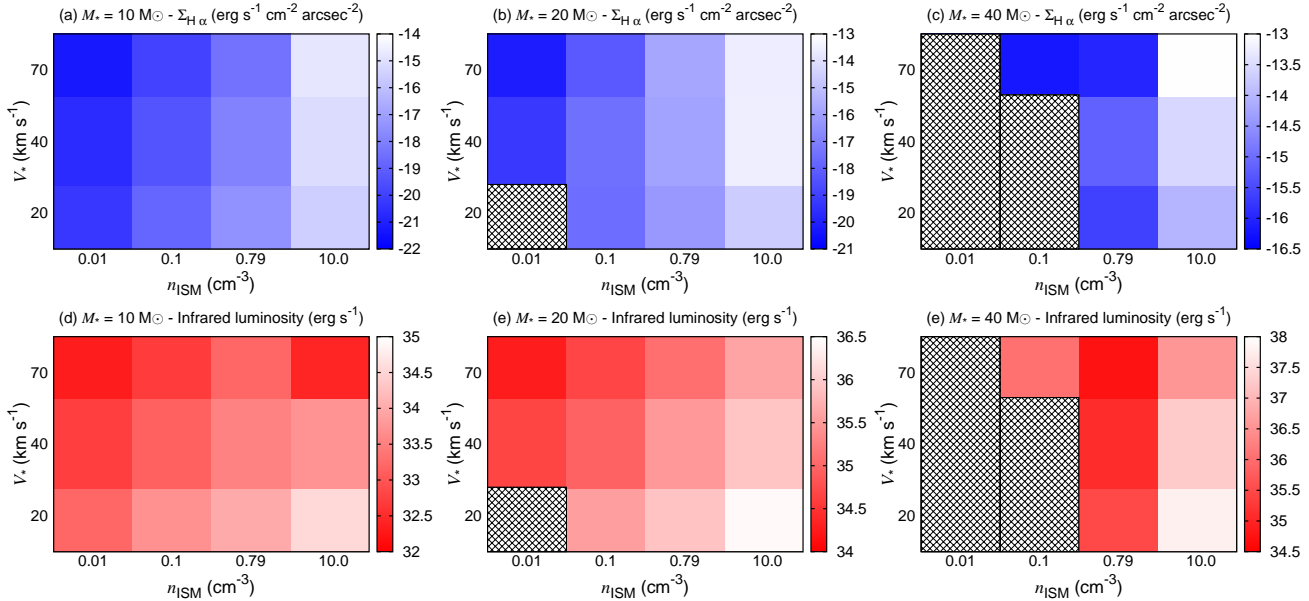


Figure 8. Bow shock $H\alpha$ surface brightness (in $\text{erg s}^{-1} \text{cm}^{-2} \text{arcsec}^{-2}$, top blue panels) and infrared reprocessed starlight (in erg s^{-1} , bottom red panels) in the logarithmic scale. We display these quantities for our models with $M_* = 10 M_\odot$ (left panels), $20 M_\odot$ (middle panels) and $40 M_\odot$ (right panels). The hatched regions indicate that the corresponding bow shock models are not included in our grid of simulations, since the duration of the main-sequence phase of these stars does not allow to generate bow shocks in a steady state at these ambient medium density. On each plot the horizontal axis is the ambient medium density n_{ISM} (in cm^{-3}) and the vertical axis is the space velocity v_* (in km s^{-1}) of our runaway stars.

star have a volume smaller than about a few pc^3 and have emission smaller than about $10^{-15} \text{erg s}^{-1} \text{cm}^{-2} \text{arcsec}^{-2}$. The models with $M_* = 20 M_\odot$ have larger volume at equal n_{ISM} and can reach surface brightness of about a few $10^{-14} \text{erg s}^{-1} \text{cm}^{-2} \text{arcsec}^{-2}$ if $n_{\text{ISM}} = 10 \text{cm}^{-3}$. Note that all models with $n_{\text{ISM}} \geq 10.0 \text{cm}^{-3}$ produce emission larger than the diffuse emission sensitivity threshold of the *SuperCOSMOS H-Alpha Survey* (SHS) of $\Sigma_{\text{SHS}} \approx 1.1\text{--}2.8 \times 10^{17} \text{erg s}^{-1} \text{cm}^{-2} \text{arcsec}^{-2}$ (Parker et al. 2005) and such bow shocks should consequently be observed by this survey (see horizontal black line in Fig. 11a).

As discussed above, a significant fraction of our sample of bow shocks models have a $H\alpha$ surface brightness larger than the sensitivity limit of the SHS survey (Parker et al. 2005). This remark can be extended to other (all-sky) $H\alpha$ observations campaigns, especially if their detection threshold is lower than the SHS. This is the case of, e.g. the *Virginia Tech Spectral-Line Survey* (VTSS, Dennison et al. 1999) and the *Wisconsin H-Alpha Mapper* (WHAM, Reynolds et al. 1998) which provide us with images of diffuse sensitivity detection limit that allow the revelation of structures associated with sub-Rayleigh intensity. Consequently, one can expect to find optical traces of stellar wind bow shocks from OB stars in these data. According to our study, their driving stars are more likely to be of initial mass $M_* \geq 20 M_\odot$ (Fig. 11a). This also implies that bow shocks *in the field* that are observed with such facilities are necessary produced by runaway stars of initial mass larger than $M_* \geq 20 M_\odot$. Moreover, we find that the models involving an $10 M_\odot$ star and with $v_* \geq 40 \text{km s}^{-1}$ have $\Sigma_{[\text{OIII}]}^{\text{max}} / \Sigma_{[\text{H}\alpha]}^{\text{max}} > 10$, whereas almost all of the other simulations do not satisfy this criterion (Fig. 11b).

Furthermore, we find a similarity between some of the cross-sections taken along the symmetry axis of the $H\alpha$ surface brightness of our bow shock models (Fig. 10) and the measure of the radial brightness in emission measure of the bow shock generated by the runaway O star HD 57061 (see fig. 5 of Brown & Bomans

2005). This observable and our model authorize a comparison since $H\alpha$ emission and emission measures have the same quadratic dependence on the gas number density. The emission measure profile of HD 57061 slightly increases from the star to the bow shock and steeply peaks in the region close to the contact discontinuity, before to decrease close to the forward shock of the bow shock and reach the ISM background emission. Our $H\alpha$ profile with $\phi = 60^\circ$ is consistent with (i) the above described variations and (ii) with the estimate of the inclination of the symmetry axis of HD 57061 with respect to the plane of the sky of about 75° , see table 3 of Brown & Bomans (2005). Note that according to our simulations, the emission peaks in the region separating the hot from the cold shocked ISM gas.

Brown & Bomans (2005) extracted a subset of 8 bow shocks at $H\alpha$ from the catalogue compiled by van Buren et al. (1995). The bow shocks of the stars HD149757 and HD158186 do not match any of our models. The O6.5V star HD17505 moving in a medium with $n_{\text{ISM}} \approx 21 \text{cm}^{-3}$ is also incompatible with the space of parameter covered by our study. The circumstellar nebulae of HD92206 ($R(0) \approx 3.67 \text{pc}$, $n_{\text{ISM}} \approx 0.007 \text{cm}^{-3}$, $v_* \approx 40.5 \text{km s}^{-1}$) and HD135240 ($R(0) \approx 3.50 \text{pc}$, $n_{\text{ISM}} \approx 0.21 \text{cm}^{-3}$, $v_* \approx 32.5 \text{km s}^{-1}$) have some of their properties similar to our models MS2040n0.01/MS2070n0.01 ($R(0) \approx 7.80\text{--}3.80 \text{pc}$, $n_{\text{ISM}} = 0.01 \text{cm}^{-3}$, $v_* = 40\text{--}70 \text{km s}^{-1}$) and MS2020n0.1/MS2040n0.1 ($R(0) \approx 3.51\text{--}2.02 \text{pc}$, $n_{\text{ISM}} = 0.1 \text{cm}^{-3}$, $v_* = 20\text{--}40 \text{km s}^{-1}$) but do not properly fit them. The bow shock of HD57061 ($R(0) \approx 7.56 \text{pc}$, $n_{\text{ISM}} \approx 0.07 \text{cm}^{-3}$, $v_* \approx 55.8 \text{km s}^{-1}$) matches particularly our model MS2040 with $R(0) \approx 7.8 \text{pc}$, $n_{\text{ISM}} = 0.01 \text{cm}^{-3}$ and $v_* = 40 \text{km s}^{-1}$, and therefore constitute a good candidate for future tailored numerical simulations. More detailed simulations and subsequent post-processing of the corresponding data, e.g. including the effects of the extinction of the ISM on the infrared emission are necessary for a more detailed discussion of these results.

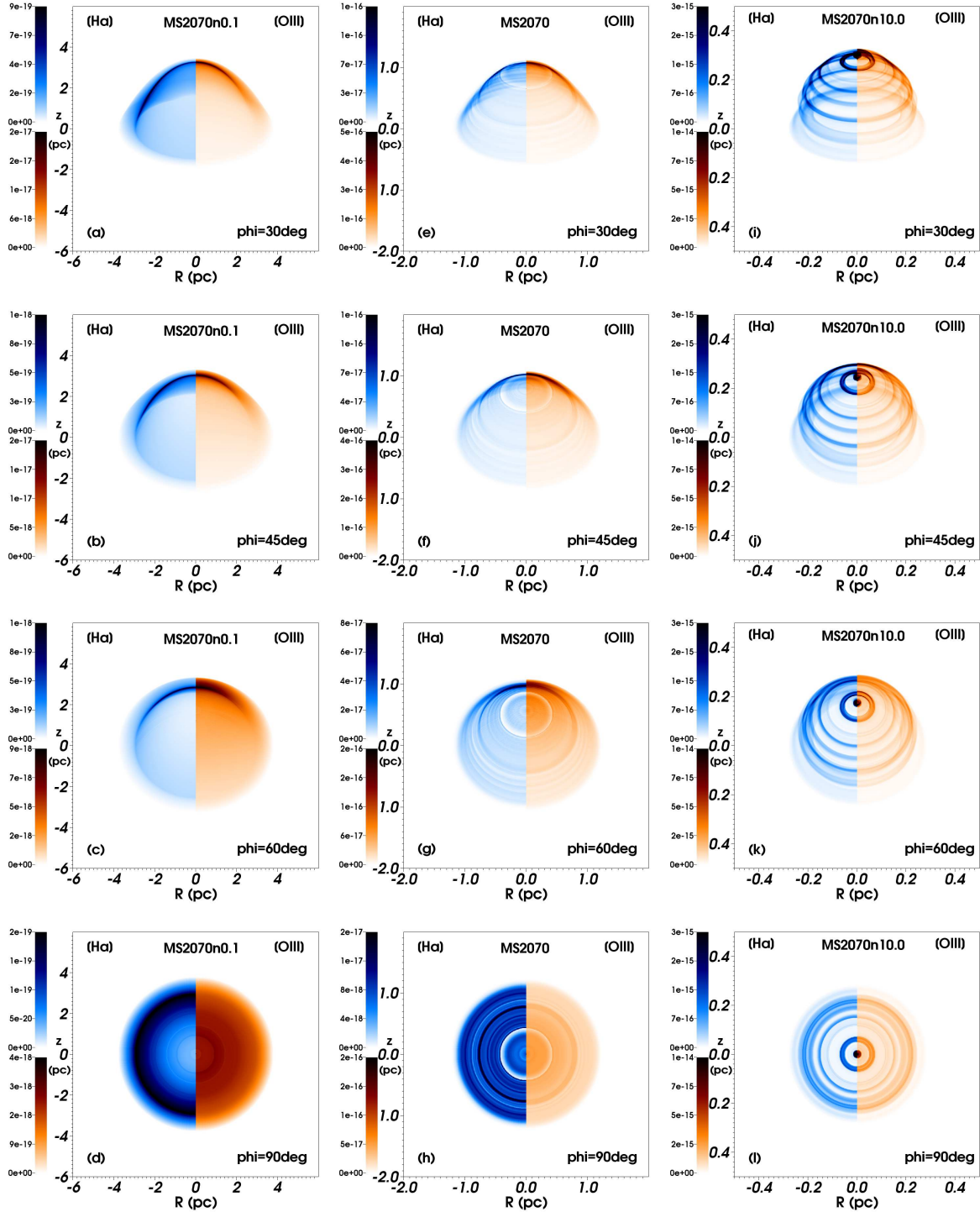


Figure 9. H α surface brightness (left, in $\text{erg s}^{-1} \text{cm}^{-2} \text{arcsec}^{-2}$) and projected [OIII] λ 5007 spectral line emission (right, in $\text{erg s}^{-1} \text{cm}^{-2} \text{arcsec}^{-2}$) of the bow shocks generated by a $20 M_{\odot}$ ZAMS star moving with velocity $v_* = 70 \text{ km s}^{-1}$ through in a medium with $n_{\text{ISM}} = 0.1$ (left column of panels a-d), 0.79 (middle column of panels e-h) and 10 cm^{-3} (right column of panels i-l). The figures correspond to an inclination angle $\phi = 30^\circ$ (top line of panels a,e,i), $\phi = 45^\circ$ (second line of panels b,f,j), $\phi = 60^\circ$ (third line of panels c,g,k) and $\phi = 90^\circ$ (bottom line of panels d,h,l) with respect to the plane of the sky. Quantities are calculated excluding the undisturbed ISM and plotted in the linear scale, as a function of the inclination angle and the ambient medium density.

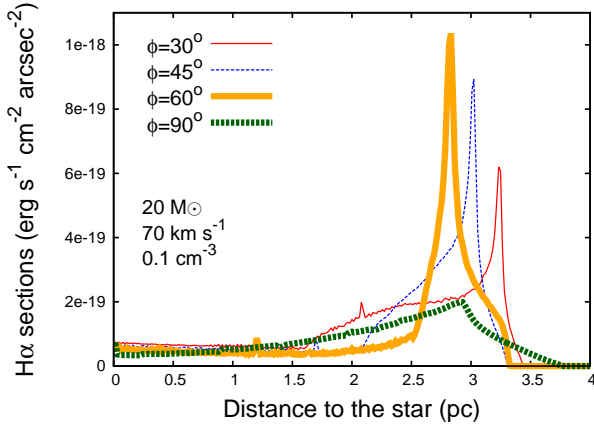


Figure 10. Cross-sections taken along the direction of motion of our $20 M_{\odot}$ ZAMS star moving with velocity 70 km s^{-1} in an ambient medium of number density $n_{\text{ISM}} = 0.1 \text{ cm}^{-3}$. The data are plotted for inclination angles $\phi = 30^{\circ}$ (thin solid red line), $\phi = 45^{\circ}$ (thin dotted blue line), $\phi = 60^{\circ}$ (thick solid orange line) and $\phi = 90^{\circ}$ (thick dotted dark green line) through their $\text{H}\alpha$ surface brightness (see Fig. 9a-d). The position of the star is located at the origin.

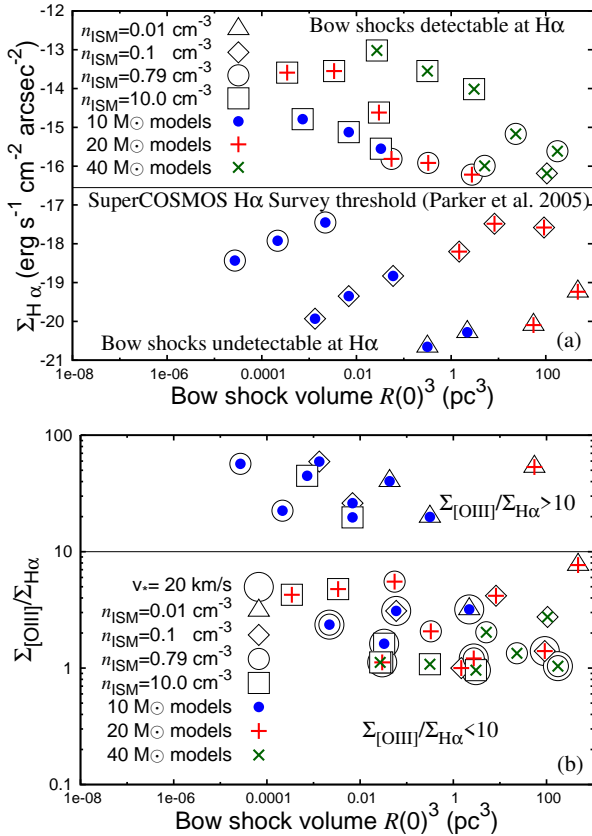


Figure 11. Bow shock $\text{H}\alpha$ surface brightness (a) and ratio $\Sigma_{[\text{OIII}]}^{\text{max}}/\Sigma_{[\text{H}\alpha]}^{\text{max}}$ (b) as a function of its volume $R(0)^3$ (in pc^3). Upper panel shows the $\text{H}\alpha$ surface brightness as a function of the detection threshold of the SuperCOSMOS $\text{H}\alpha$ Survey (SHS) of $\Sigma_{\text{SHS}} \approx 1.1 - 2.8 \times 10^{-17} \text{ erg s}^{-1} \text{ cm}^{-2} \text{ arcsec}^{-2}$ (Parker et al. 2005). Lower panel plots the ratio $\Sigma_{[\text{OIII}]}^{\text{max}}/\Sigma_{[\text{H}\alpha]}^{\text{max}}$ of the same models.

4.3.4 Implication for the evolution of supernova remnants generated by massive runaway stars

Massive stars evolve and die as supernovae, a sudden and strong release of matter, energy and momentum taking place inside the ISM pre-shaped by their past stellar evolution (Langer 2012). In the case of a runaway progenitor, the circumstellar medium at the pre-supernova phase can be a bow shock nebula with which the shock wave interacts before expanding further into the unperturbed ISM (Brighenti & D’Ercole 1994). The subsequent growing supernova remnant develops asymmetries since it is braked by the mass at the apex of the bow shock but expands freely in the cavity driven by the star in the opposite direction (Borkowski et al. 1992). If the progenitor is slightly supersonic, the bow shock is mainly shaped during the main-sequence phase of the star; whereas if the progenitor is a fast-moving star then the bow shock is essentially made of material from the last pre-supernova evolutionary phase. In the Galactic plane ($n_{\text{ISM}} = 0.79 \text{ cm}^{-3}$) such asymmetries arise if the apex of the bow shock accumulates at least $1.5 M_{\odot}$ of shocked material (Meyer et al. 2015).

In Fig. 12 we present the mass trapped into the $z \geq 0$ region of our bow shock models as a function of their volume. As in Fig. 11 the figure distinguishes the initial mass and the ambient medium density of each models. Amongst our bow shock simulations, 9 models have $M_{\text{bow}} \gtrsim 1.5 M_{\odot}$ and 4 of them are generated by the runaway stars which asymmetric supernova remnant studied in detail in Meyer et al. (2015). The other models with $v_* \leq 40 \text{ km s}^{-1}$ may produce asymmetric remnants because they will explode inside their main-sequence wind bubble. The model MS4070n0.1 has $v_* = 70 \text{ km s}^{-1}$ which indicates that the main-sequence bow shock will be advected downstream by the rapid stellar motion and the surroundings of the progenitor at the pre-supernova phase is made of, e.g. red supergiant material. Consequently, its shock wave may be unaffected by the presence of the circumstellar medium. We leave the examination via hydrodynamical simulations of this conjecture for future works. Interestingly, we notice that most of the potential progenitors of asymmetric supernova remnants are moving in a low density medium $n_{\text{ISM}} \leq 0.1 \text{ cm}^{-3}$, i. e. in the rather high latitude regions of the Milky Way. This is consistent with the interpretation of the elongated shape of, e.g. Kepler’s supernova remnant as the consequence of the presence of a massive bow shock at the time of the explosion (Velázquez et al. 2006; Toledo-Roy et al. 2014).

4.3.5 The influence of the interstellar magnetic field on the shape of supernovae remnants

An alternative explanation for the asymmetrical shape of supernova remnants can be found in the influence of the interstellar magnetic field. Although the interstellar magnetic field does not influence the shape of an expanding supernova blast wave directly (Manchester 1987) it can influence the shape and size of the wind-blown bubble, as suggested by Arnal (1992) and shown numerically by van Marle et al. (2015). Such magnetic fields slow the expansion of the wind-blown bubble in the direction perpendicular to the direction of the field and, depending on the field strength can stop the expansion in that direction completely. The end result is an elongated, ellipsoid bubble, which in turn, would influence the expansion of the supernova remnant.

As shown by van Marle et al. (2015), the interstellar magnetic field would have to be fairly strong (beyond about $20 \mu\text{G}$) to enable it to constrain the wind-bubble sufficiently that the

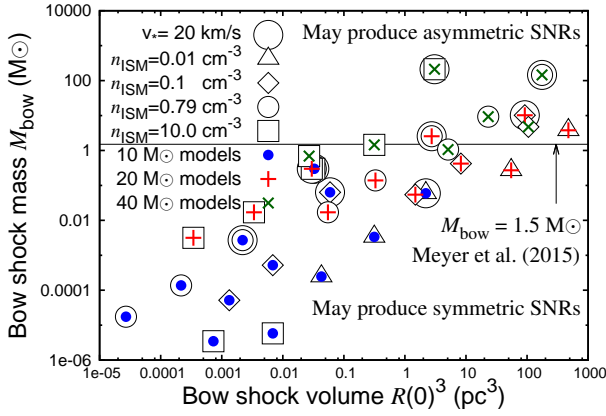


Figure 12. Bow shocks mass as a function of the bow shock volume. The figure shows the mass M_{bow} (in M_{\odot}) trapped in the $z \geq 0$ region of the bow shock as a function of its volume $R(0)^3$ (in pc^3). The dots distinguish between models (i) as a function of the ISM ambient medium with $n_{\text{ISM}} = 0.01$ (triangles), 0.1 (diamonds), 0.79 (circles) and 10 cm^{-3} (squares), and (ii) as a function of the initial mass of the star with 10 (blue dots), 20 (red plus signs) and $40 M_{\odot}$ (green crosses). The thin horizontal black line corresponds to $M_{\text{bow}} = 1.5 M_{\odot}$, i.e. the condition to produce an asymmetric supernova remnant if $n_{\text{ISM}} = 0.79 \text{ cm}^{-3}$ (Meyer et al. 2015).

scale of the bubble would be reduced to that of a bow shock. However, such field-strengths are not unreasonable as field strengths of up to $60 \mu\text{G}$, have been observed in the galactic core (Rand & Kulkarni 1989; Ohno & Shibata 1993; Frick et al. 2001; Opher et al. 2009; Shabala et al. 2010; Fletcher et al. 2011; Heerikhuisen & Pogorelov 2011; Vallée 2011) and fields that are stronger than that by an order of magnitude can be found inside molecular clouds (Crutcher et al. 1999).

There are two tests that can be used to distinguish whether the bubble into which a supernova remnant expands has been constrained by stellar motion, or by an interstellar magnetic field. One: the magnetic field in the galaxy tends to be aligned with the spiral arms. Gaensler (1998) showed that supernova remnants tend to be aligned with the galactic disk. This would seem to support the theory that it is the magnetic field, rather than a bow shock, that constrained the wind expansion. However, the correlation is not very strong. Two: the shape of the supernova remnant itself. Van Marle (2015) showed that a supernova remnant, expanding inside a magnetically constrained bubble, first collides with the outer edge along the minor axis of the ellipsoid bubble, while, in the direction along the major axis the expansion can continue uninterrupted. This produces a barrel-like supernova remnant. When expanding inside a bow shock, the collision would first occur at the front of the bow shock, creating a parabolic shape with free expansion only possible along the tail of the bow shock.

5 CONCLUSION

Our bow shock simulations indicate that no structural difference arise when changing the density of the background ISM in which the stars move, i.e. their internal organisation is similar as described in Comerón & Kaper (1998) and Paper I. The same is true for their radiative properties, governed by line cooling such as the [OIII] $\lambda 5007$ line and showing faint $\text{H}\alpha$ emission, both principally originating from outer region of shocked ISM gas. We also find that

their X-rays signature is fainter by several orders of magnitude than their $\text{H}\alpha$ emission, and, consequently, it is not a good waveband to search for such structures.

The best way to observe bow shocks remains their infrared emission of starlight reprocessed by shocked ISM dust (Meyer et al. 2014). We find that the brightest infrared bow shocks, i.e. the most easily observable ones, are produced by high-mass ($M_{\star} \approx 40 M_{\odot}$) stars moving with a slow velocity ($v_{\star} \approx 20 \text{ km s}^{-1}$) in the relatively dense regions ($n_{\text{ISM}} \approx 10 \text{ cm}^{-3}$) of the ISM, whereas the brightest $\text{H}\alpha$ structures are produced by these stars when moving rapidly ($v_{\star} \approx 70 \text{ km s}^{-1}$). Thin-shelled bow shocks have mid-infrared luminosities which does not report the time-variations of their unstable structures. This indicates that spectral energy distributions of stellar wind bow shocks are the appropriate tool to analyze them since they do not depend on the temporary effects that affect their density field. We find that bow shocks from Galactic runaway stars have emission peaking in the wavelength range $3 \leq \lambda \leq 50 \mu\text{m}$. Interestingly, the circumstellar material can be up to several orders of magnitude brighter than the star and dominates the emission, especially if $M_{\star} \geq 20 M_{\odot}$.

A detailed analysis of our grid of simulations indicates that the $\text{H}\alpha$ surface brightness of Galactic stellar wind bow shocks increases if their angle of inclination with respect to the plane of the sky increases up to $\phi = 60^\circ$, however, edge-on viewed bow shocks are particularly faint. We find that all bow shocks generated by a $40 M_{\odot}$ ZAMS runaway star could be observed with Rayleigh-sensitive $\text{H}\alpha$ facilities and that bow shocks observed *in the field* by means of these facilities should have an initial mass larger than about $20 M_{\odot}$. Furthermore, all of our bow shocks generated by a $10 M_{\odot}$ ZAMS star moving with $v_{\star} \geq 40 \text{ km s}^{-1}$ have a line ratio $\Sigma_{[\text{OIII}]}^{\text{max}} / \Sigma_{[\text{H}\alpha]}^{\text{max}} > 10$. Our study suggests that slowly-moving stars of ZAMS mass $M_{\star} \geq 20 M_{\odot}$ moving in a medium of $n_{\text{ISM}} \geq 0.1 \text{ cm}^{-3}$ generate massive bow shocks, i.e. are susceptible to induce asymmetries in their subsequent supernova shock wave. This study will be enlarged, e.g. estimating observability of red supergiant stars.

ACKNOWLEDGEMENTS

We thank the anonymous referee for numerous comments which greatly improved both the quality and the presentation of the paper. D. M.-A. Meyer thanks P. F. Velazquez, F. Brighenti and L. Kaper for their advices, and F. P. Wilkin for useful comments on stellar wind bow shocks which partly motivated this work. This study was conducted within the Emmy Noether research group on “Accretion Flows and Feedback in Realistic Models of Massive Star Formation” funded by the German Research Foundation under grant no. KU 2849/3-1. A.-J. van Marle acknowledges support from FWO, grant G.0227.08, KU Leuven GOA/2008, 04 and GOA/2009/09. The authors gratefully acknowledge the computing time granted by the John von Neumann Institute for Computing (NIC) and provided on the supercomputer JUROPA at Jülich Supercomputing Centre (JSC).

REFERENCES

- Adams J. D., Herter T. L., Gull G. E., Schoenwald J., Keller L. D., Berthoud M., Stacy G. J., Nikola T., Henderson C. P., 2008, in Society of Photo-Optical Instrumentation Engineers (SPIE) Conference Series Vol. 7014 of Society of Photo-Optical Instrumentation Engineers (SPIE) Conference Series, FORCAST: the first light instrument for SOFIA. p. 2

- Arnal E. M., 1992, *A&A*, 254, 305
- Arnaud K. A., 1996, in Jacoby G. H., Barnes J., eds, *Astronomical Data Analysis Software and Systems V* Vol. 101 of *Astronomical Society of the Pacific Conference Series*, XSPEC: The First Ten Years. p. 17
- Asplund M., Grevesse N., Sauval A. J., Scott P., 2009, *ARA&A*, 47, 481
- Blaauw A., 1961, *Bull. Astron. Inst. Netherlands*, 15, 265
- Blondin J. M., Koerwer J. F., 1998, *New Ast.*, 3, 571
- Borkowski K. J., Blondin J. M., Sarazin C. L., 1992, *ApJ*, 400, 222
- Brandl B., Lenzen R., Venema L., Käufel H.-U., Finger G., Glasse A., Brandner W., Stuik R., 2006, in *Society of Photo-Optical Instrumentation Engineers (SPIE) Conference Series* Vol. 6269 of *Society of Photo-Optical Instrumentation Engineers (SPIE) Conference Series*, MIDIR-TOWL: the thermal/mid-IR instrument for the E-ELT. p. 20
- Brighenti F., D'Ercole A., 1994, *MNRAS*, 270, 65
- Brighenti F., D'Ercole A., 1995, *MNRAS*, 277, 53
- Brott I., de Mink S. E., Cantiello M., Langer N., de Koter A., Evans C. J., Hunter I., Trundle C., Vink J. S., 2011, *A&A*, 530, A115
- Brown D., Bomans D. J., 2005, *A&A*, 439, 183
- Comerón F., Kaper L., 1998, *A&A*, 338, 273
- Comerón F., Pasquali A., 2007, *A&A*, 467, L23
- Cowie L. L., McKee C. F., 1977, *ApJ*, 211, 135
- Crutcher R. M., Roberts D. A., Troland T. H., Goss W. M., 1999, *ApJ*, 515, 275
- de Jager C., Nieuwenhuijzen H., van der Hucht K. A., 1988, *A&AS*, 72, 259
- Decin L., Hony S., de Koter A., Justtanont K., Tielens A. G. G. M., Waters L. B. F. M., 2006, *A&A*, 456, 549
- Dennison B., Simonetti J. H., Topasna G. A., 1999, in *American Astronomical Society Meeting Abstracts* Vol. 31 of *Bulletin of the American Astronomical Society*, The Virginia Tech H-alpha and [SII] Imaging Survey of the Northern Sky. p. 1455
- Diaz-Miller R. I., Franco J., Shore S. N., 1998, *ApJ*, 501, 192
- Dopita M. A., 1973, *A&A*, 29, 387
- Dyson J. E., 1975, *Ap&SS*, 35, 299
- Eldridge J. J., Langer N., Tout C. A., 2011, *MNRAS*, 414, 3501
- Fletcher A., Beck R., Shukurov A., Berkhuijsen E. M., Horellou C., 2011, *MNRAS*, 412, 2396
- Frick P., Stepanov R., Shukurov A., Sokoloff D., 2001, *MNRAS*, 325, 649
- Gaensler B. M., 1998, *ApJ*, 493, 781
- Garcia-Segura G., Mac Low M.-M., Langer N., 1996, *A&A*, 305, 229
- Gull T. R., Sofia S., 1979, *ApJ*, 230, 782
- Gvaramadze V. V., Bomans D. J., 2008, *A&A*, 490, 1071
- Heerikhuisen J., Pogorelov N. V., 2011, *ApJ*, 738, 29
- Heger A., Woosley S. E., Spruit H. C., 2005, *ApJ*, 626, 350
- Henney W. J., Arthur S. J., de Colle F., Mellema G., 2009, *MNRAS*, 398, 157
- Holzer T. E., Axford W. I., 1970, *ARA&A*, 8, 31
- Hoogerwerf R., de Bruijne J. H. J., de Zeeuw P. T., 2001, *A&A*, 365, 49
- Hummer D. G., 1994, *MNRAS*, 268, 109
- Huthoff F., Kaper L., 2002, *A&A*, 383, 999
- Kaneda H., Nakagawa T., Onaka T., Matsumoto T., Murakami H., Enya K., Kataza H., Matsuhara H., Yui Y. Y., 2004, in *Mather J. C., ed., Optical, Infrared, and Millimeter Space Telescopes* Vol. 5487 of *Society of Photo-Optical Instrumentation Engineers (SPIE) Conference Series*, Development of space infrared telescope for the SPICA mission. pp 991–1000
- Kaper L., van Loon J. T., Augusteijn T., Goudfrooij P., Patat F., Waters L. B. F. M., Zijlstra A. A., 1997, *ApJ*, 475, L37
- Kudritzki R. P., Pauldrach A., Puls J., Abbott D. C., 1989, *A&A*, 219, 205
- Kuiper R., Klahr H., Beuther H., Henning T., 2012, *A&A*, 537, A122
- Langer N., 2012, *ARA&A*, 50, 107
- Manchester R. N., 1987, *A&A*, 171, 205
- Meyer D. M.-A., Gvaramadze V. V., Langer N., Mackey J., Boumis P., Mohamed S., 2014, *MNRAS*, 439, L41
- Meyer D. M.-A., Langer N., Mackey J., Velázquez P. F., Gusdorf A., 2015, *MNRAS*, 450, 3080
- Meyer D. M.-A., Mackey J., Langer N., Gvaramadze V. V., Mignone A., Izzard R. G., Kaper L., 2014, *MNRAS*, 444, 2754
- Mignone A., Bodo G., Massaglia S., Matsakos T., Tesileanu O., Zanni C., Ferrari A., 2007, *ApJS*, 170, 228
- Mignone A., Zanni C., Tzeferacos P., van Straalen B., Colella P., Bodo G., 2012, *ApJS*, 198, 7
- Mohamed S., Mackey J., Langer N., 2012, *A&A*, 541, A1
- Neugebauer G., Habing H. J., van Duinen R., Aumann H. H., Baud B., Beichman C. A., Beintema D. A., Boggess N., Clegg P. E., de Jong T., Emerson J. P., Gautier T. N., Gillett F. C., Harris S., Hauser M. G., Houck J. R., Jennings R., 1984, *ApJ*, 278, L1
- Noriega-Crespo A., van Buren D., Cao Y., Dgani R., 1997, *AJ*, 114, 837
- Noriega-Crespo A., van Buren D., Dgani R., 1997, *AJ*, 113, 780
- Ohno H., Shibata S., 1993, *MNRAS*, 262, 953
- Opher M., Bibi F. A., Toth G., Richardson J. D., Izmodenov V. V., Gombosi T. I., 2009, *Nature*, 462, 1036
- Osterbrock D. E., Bochkarev N. G., 1989, *Soviet Ast.*, 33, 694
- Parker Q. A., Phillipps S., Pierce M. J., Hartley M., Hambly N. C., Read M. A., MacGillivray 2005, *MNRAS*, 362, 689
- Peri C. S., Benaglia P., Brookes D. P., Stevens I. R., Isequilla N. L., 2012, *A&A*, 538, A108
- Peri C. S., Benaglia P., Isequilla N. L., 2015, *A&A*, 578, A45
- Peters T., Banerjee R., Klessen R. S., Mac Low M.-M., Galván-Madrid R., Keto E. R., 2010, *ApJ*, 711, 1017
- Petrovic J., Langer N., Yoon S.-C., Heger A., 2005, *A&A*, 435, 247
- Petrovic J., Pols O., Langer N., 2006, *A&A*, 450, 219
- Rand R. J., Kulkarni S. R., 1989, *ApJ*, 343, 760
- Reynolds R. J., Tuftte S. L., Haffner L. M., Jaehnig K., Percival J. W., 1998, *Publ. Astron. Soc. Aust.*, 15, 14
- Rozyczka M., Tenorio-Tagle G., Franco J., Bodenheimer P., 1993, *MNRAS*, 261, 674
- Shabala S. S., Mead J. M. G., Alexander P., 2010, *MNRAS*, 405, 1960
- Spitzer L., 1962, *Physics of Fully Ionized Gases*
- Spitzer L., 1978, *Physical processes in the interstellar medium*
- Swinyard B. M., Rieke G. H., Ressler M., Glasse A., Wright G. S., Ferlet M., Wells M., 2004, in *Mather J. C., ed., Optical, Infrared, and Millimeter Space Telescopes* Vol. 5487 of *Society of Photo-Optical Instrumentation Engineers (SPIE) Conference Series*, Sensitivity estimates for the mid-infrared instrument (MIRI) on the JWST. pp 785–793
- Thun D., Kuiper R., Schmidt F., Kley W., 2016, *ArXiv e-prints*:1601.07799
- Toledo-Roy J. C., Esquivel A., Velázquez P. F., Reynoso E. M., 2014, *MNRAS*, 442, 229
- Vallée J. P., 2011, *New Astronomy Reviews*, 55, 23
- van Buren D., McCray R., 1988, *ApJ*, 329, L93
- van Buren D., Noriega-Crespo A., Dgani R., 1995, *AJ*, 110, 2914
- van Marle A. J., Decin L., Meliani Z., 2014, *A&A*, 561, A152
- van Marle A. J., Langer N., García-Segura G., 2007, *A&A*, 469, 941
- van Marle A. J., Meliani Z., Keppens R., Decin L., 2011, *ApJ*, 734, L26
- van Marle A. J., Meliani Z., Marcowith A., 2015, *A&A*, 584, A49
- van Veelen B., 2010, PhD thesis, Utrecht University, Netherland
- Velázquez P. F., Vigh C. D., Reynoso E. M., Gómez D. O., Schneider E. M., 2006, *ApJ*, 649, 779
- Villaver E., Machado A., García-Segura G., 2012, *ApJ*, 748, 94
- Vishniac E. T., 1994, *ApJ*, 428, 186
- Weaver R., McCray R., Castor J., Shapiro P., Moore R., 1977, *ApJ*, 218, 377
- Wiersma R. P. C., Schaye J., Smith B. D., 2009, *MNRAS*, 393, 99
- Wilkin F. P., 1996, *ApJ*, 459, L31
- Woosley S. E., Heger A., Weaver T. A., 2002, *Reviews of Modern Physics*, 74, 1015
- Wright E. L., Eisenhardt P. R. M., Mainzer A. K., Ressler M. E., Cutri R. M., Jarrett T., Kirkpatrick J. D., Padgett D., McMillan R. S., Skrutskie M., Stanford S., 2010, *AJ*, 140, 1868
- Yoon S.-C., Langer N., 2005, *A&A*, 443, 643